DALHOUSIE UNIVERSITY

Effect of the Metal Substrate on Interlayer Interactions in Bilayer Graphene

Matthew S. Christian and Erin R. Johnson*

Department of Chemistry, Dalhousie University, 6274 Coburg Road, Halifax, Nova Scotia, Canada B3H 4R2

E-mail: erin.johnson@dal.ca

Abstract

Bilayer graphene (BLG) has been shown to have advantageous electronic and physical properties relative to single-layer graphene (SLG) and is a model system for probing the tribology of graphene-based lubricants. However, few studies have investigated how metal substrates affect interlayer interactions, as quantified by the exfoliation energy and the sliding barrier of the upper graphene layer. In this work, we present a study of adsorbed BLG on several transition-metal surfaces using density-functional theory (DFT) incorporating the exchange-hole dipole moment (XDM) dispersion model. Our results show that physisorption of BLG on a surface does not significantly perturb the interlayer interactions, exfoliation, or sliding. Conversely, chemisorption of BLG increases the exfoliation energy and decreases the sliding barriers due to stronger dispersion contributions from the metal substrate. Changes in translational and rotational orientations massively impact the sliding friction for Ni-group metals that can facilitate both chemisorption and physisorption.

*To whom correspondence should be addressed

1 Introduction

Due to its unique two-dimensional electronic structure, graphene has attracted a great deal of recent attention for its wide range of of potential device applications. A common route to graphene synthesis involves chemical vapor deposition on metal substrates, which can result in formation of adsorbed single-layer graphene (SLG) or bilayer graphene (BLG).[1–6] Few-layer graphene is an excellent friction modifier for metal contacts as its properties lead to a high lubricity, reducing the sliding barrier relative to that of the unadorned bimetallic interface.[7–9]

The interaction of graphene with metal surfaces varies with substrate type and lattice commensurability.[2,10] Graphene can either physisorb, bound by weak dispersion interactions,[11–13] or chemisorb, bound by a combination of electrostatic and dispersion interactions.[14,15] Physisorption is characterized by SLG–metal interlayer distances of >3Å and effectively zero charge transfer, as occurs for Al and the Cu-group metals.[16] Alternatively, graphene can either physisorb on chemisorb on Ni-group metals, depending on the rotational orientation. Chemisorption is characterized by interlayer distances of < 2.5Å and significant charge transfer.[16]

Tribologists have studied substrate effects on bilayer sliding,[17–23] demonstrating that the energy barriers are dependent on the number of graphene layers and on the strength of their surface adhesion. In general, the friction tends to decrease with increasing numbers of layers,[22,23] as this increases the smoothness of the graphene. Similarly, strong interactions with the substrate result in smoother graphene layers and decrease the sliding barrier, while weak interactions lead to increased roughness or corrugation and cause greater friction.[20–22] However, relatively little is known regarding how an underlying metal substrate can affect the adsorption and frictional properties of the upper graphene layer in adsorbed BLG beyond such changes in roughness.

Investigations of friction on highly-planar graphene surfaces can be conducted using a quartz crystal microbalance (QCM), rather than by atomic force microscopy (AFM) where

the tip causes graphene wrinkling. QCM studies have examined adsorption and friction of noble-gas atoms on graphene/Ni(111) surfaces[24] and found the effect of the underlying substrate to be negligible.[25] However, this is at odds with combined DFT and Raman-spectroscopy results that a hexagonal boron nitride substrate strengthens the adsorption of molecular bromine on graphene.[26] Additionally, a further QCM study found a significantly greater interaction strength between gold nanocrystals a graphite substrate compared to SLG graphene.[27]

Several previous computational studies investigated BLG adsorbed on various metal surfaces, but either concentrated on carbon-metal distances and energies rather than interactions between the graphene layers,[28,29] or used the local density approximation,[30] which lacks a treatment of dispersion interactions needed to describe these systems. A study of BLG adsorbed on the Cu and Ni (111) surfaces using PBE functional[31] and the D2 dispersion correction[32] found that the interlayer interaction is significantly stronger on Ni, relative to freestanding BLG.[33] Another PBE-D2 study found that a Ni(111) substrate both increases interlayer adhesion and decreases the lateral sliding force for trilayer graphene.[7]

Use of a density-dependent dispersion correction has been shown to yield far more accurate graphene-metal distances and energetics[16,34] than the empirical dispersion corrections used in previous BLG studies.[7,33] The exchange-hole dipole moment (XDM) model,[35,36] is a non-empirical dispersion correction that uses the electron density to generate C_6 (and higher-order) dispersion coefficients. These dispersion coefficients are used to evaluate the dispersion energy between all pairs of atoms, i and j:

$$E_{\mathrm{XDM}} = -\frac{1}{2}\sum_{n=6,8,10}\sum_{i\neq j}\frac{C_{n,ij}f_n(R_{ij})}{R_{ij}^n}, \tag{1}$$

where R_{ij} is the interatomic distance and f_n is a damping function that attenuates the dispersion correction at short range. Each pairwise-atomic dispersion coefficient, $C_{n,ij}$, is determined from integrals involving the exchange-hole multipole moments for the interacting

atoms, as well as the atom-in-molecule polarizabilities. The XDM dispersion energy is added to the base DFT energy as a post-SCF correction:

$$E = E_{\text{base}} + E_{\text{XDM}}. \tag{2}$$

The non-empirical and environment-dependent nature of the dispersion coefficients allows XDM to model dispersion interactions accurately for diverse systems ranging from molecular dimers to supra-molecular systems to organic crystals.[36] Most relevant to this paper, XDM has been shown to accurately model physisorption of molecules[37] and of SLG[16,34] on metal surfaces.

This article is the first to systematically consider substrate effects on bilayer graphene for the late transition metals with state-of-the-art dispersion-corrected DFT methods. It represents the third part of an investigative series on graphene-metal interactions using DFT paired with the XDM dispersion correction.[16,34] In this work, we investigate if and how metal substrates affect BLG interfacial distances and interaction energies, as well as energy barriers for interlayer sliding. In the first section, we compare properties of BLG with graphite as a reference to gauge how the graphite substrate affects BLG energies and distances. In the remainder of the article, we consider BLG adsorbed on the (111) surface for seven metals in two rotational orientations. The second section assesses how the metal substrates affect exfoliation energies for the upper graphene layer, while the third section investigates how the substrates affect the energy barriers for interlayer sliding of the adsorbed BLG. Our results show that the substrate does significantly affect the energetics and interlayer distances of BLG for cases where the lower graphene layer is chemisorbed on the metal due to stronger dispersion attraction between the substrate surface and the upper graphene layer.

2 Computational Methods

As in our previous publications on graphene-metal interactions,[16,34] all DFT calculations were carried out using periodic boundary conditions with the projector augmented wave (PAW) formalism[38] as implemented in Quantum ESPRESSO.[39] The B86bPBE[40] exchange-correlation functional was used as it provides the best accuracy when paired with the XDM dispersion model.[41,42] An $8 \times 8 \times 1$ Γ-centered **k**-point grid was used, with a plane-wave cutoff of 60 Ry and a density expansion cutoff of 800 Ry. Cold smearing[43] was employed with a smearing parameter of 0.01 Ry.

The metal substrates considered here are the same as in our previous paper:[16] aluminum, copper, silver, gold, nickel, palladium, and platinum. Calculations for the Ni-group metals used an initial spin-polarization. All metals have a face-centered cubic (fcc) crystal structure and we consider only the (111) surface. The 0° and 30° rotational orientations, or Moiré patterns are considered for all cases except for Cu and Ni, where only the 0° orientation is considered due to the excessive compression of the adsorbed graphene that would occur in the 30° orientation.[16] The (1×1) surface unit cell is used for the 0° orientation, where the lattice vector of graphene and the metal are aligned, and the $(\sqrt{3} \times \sqrt{3})$ unit cell is used for the 30° orientation, where the graphene surface vector is rotated about the metal lattice vector by this angle. Adsorption of graphene in the 30° orientation is more stable for Al, Ag, Au, Pd, and Pt due to better lattice commensurability. However, this orientation does not allow for chemisorption, which occurs in the 0° case for Pd and Pt.[16] While many other Moiré patterns are possible experimentally, they would require much larger units cells in the DFT modeling and hence are not considered.

For the (1×1) cell, six unique translational orientations of SLG graphene layer, with respect to the metal, are possible.[16] In this work, only the minimum-energy of these orientations are considered and were used to define the configuration of the lower graphene layer in contact with the surface. These are top-hcp for Al; top-fcc for Ni, Cu, Ag, and Au; and bridge-top for Pd and Pt.[16] For nickel, we consider the chemisorption minimum favored

after inclusion of thermal-expansion effects.[34] Additionally, we also studied the chemisorbed top-fcc orientations of graphene for Pd and Pt in the (1×1) cell for consistency with the other metals and because graphene has been seen to have a combination of the bridge-top and top-fcc orientations experimentally.[44–47] Finally, calculations were also performed for freestanding BLG and for BLG adsorbed on a graphite surface.

Each surface is modeled as a slab containing six layers of metal atoms, or six layers of carbon atoms for the graphite substrate. A sufficiently large vacuum region was inserted between the slabs to separate the periodic images, yielding unit-cells 70 Bohr in length. BLG is adsorbed on the surface, with the lower layer in the orientations described above. The carbon-metal distances for this layer were set to the optimum values from our previous paper[16] and were held fixed in all subsequent calculations to simplify computation of the exfoliation and sliding potential-energy surfaces (PES). For each combined BLG-metal system, the (x, y)-unit-cell dimensions, which control the surface lattice constants, were systematically varied in 0.01 Å increments and the minimum-energy geometry obtained from quadratic interpolation. These optimum values of the lattice constants are given in Table 1 and were also held fixed in all subsequent PES calculations. Alternatively, instead of optimizing the lattice constant for the combined BLG-metal system, PES were also generated using substrate lattice constants fixed to the experimental values (see Table 1 in Ref. 16); the results are effectively identical and are presented for comparison in the Supporting Information.

Table 1 shows a comparison of the optimum lattice constants for the combined BLG-metal system with those of freestanding BLG, which demonstrates the magnitude of the lattice strain. The strain energies resulting from this lattice distortion for a single graphene layer, also reported in Table 1, are

$$E_{\text{strain}} = E_{\text{SLG}}(a_{\text{surf}}) - E_{\text{SLG}}, \tag{3}$$

where the latter value corresponds to the minimum energy for SLG. The values of the strain

Table 1: Comparison of calculated surface lattice constants (a_{surf} in Å) for BLG adsorbed on the (111) surface of selected metals for the (1×1) and $(\sqrt{3} \times \sqrt{3})$ unit cells. Also shown are the differences in lattice constant, relative to graphite (Δa_{surf} in Å), and the strain energies resulting from the changes in lattice constant for a single-layer graphene (E_{strain} in kJ/mol per C).

Metal	(1×1)			$(\sqrt{3} \times \sqrt{3})$		
	a_{surf}	Δa_{surf}	E_{strain}	a_{surf}	Δa_{surf}	E_{strain}
Al	2.66	0.19	33.9	4.95	0.00	0.1
Cu	2.51	0.04	1.8	—	—	—
Ag	2.76	0.29	68.0	4.98	0.03	1.2
Au	2.80	0.33	88.0	5.02	0.07	2.2
Ni	2.47	0.00	0.1	—	—	—
Pd	2.71[a]	0.24[a]	47.7	4.88	-0.07	0.7
	2.70[b]	0.23[b]	46.0			
Pt	2.75[a]	0.28[a]	64.1	4.90	-0.05	0.5
	2.74[b]	0.27[b]	60.1			
SLG	2.47			4.95		

The lower graphene layer is: [a]chemisorbed, bridge-top; [b]chemisorbed, top-fcc.

energy are quite high for Al, Ag, Au, Pd, and Pt in the (1×1) cell (or 0° Moiré pattern), where there is a large lattice mismatch. However, these aligned orientations are still considered as they facilitate graphene chemisorption[16] and are seen experimentally for Au, Pd, and Pt, where the graphene distorts over large length scales to reduce the lattice strain.[13,47–53]

Potential energy curves for adsorption/exfoliation of the upper graphene layer were computed to assess the strength of the BLG interlayer interaction for all substrates. The exfoliation PES were generated by translating the upper graphene layer in the z-direction, with respect to the surface, while fixing all other geometric parameters. The adsorption energy of the upper graphene layer is defined relative to the infinitely-separated, strained components, as in our previous paper.[16] Potential energy surfaces for interlayer sliding of BLG were also computed for all substrates and orientations. Starting from the minimum-energy structures, the top graphene layer was translated diagonally across the unit cell to generate the PES. This allows for the entire sliding PES to be sampled while minimizing the number of calculations by exploiting graphene's symmetry. For each point, the z-position of the upper

graphene layer was varied in 0.05 Å increments and the minimum-energy PES obtained from quadratic interpolation. Because we are interested in the relative energies along the sliding PES, we define the energies with respect to the most stable geometry for each substrate.

3 Results and Discussion

3.1 Comparison of Bilayer Graphene versus Graphite

We begin by considering the differences between BLG and graphite as a reference to understand basic substrate effects. Figure 1(a) shows a comparison of the potential energy surfaces for exfoliation of the upper graphene layer in BLG and in graphite, while Figure 1(b) shows a decomposition of these PES into base-functional and dispersion contributions. The base-functional contribution is entirely repulsive along the PES, as expected from analogy to the benzene dimer.[54] The base-functional contribution can be thought of as describing the Pauli repulsion between the graphene sheets and is off-set by dispersion to give binding in the overall PES. From Figure 1(a), the magnitude of the exfoliation energy for BLG is 0.5 kJ/mol C less than for the graphite slab, demonstrating that the graphite support causes stronger interlayer binding. Figure 1(b) reveals that the increased binding is due to additional dispersion interactions with the underlying substrate in the graphite case. This is in agreement with a combined QCM and molecular-dynamics study that found that a reduced Lennard-Jones interaction strength was needed to reproduce experimental results for a graphene substrate, relative to graphite.[27] The stronger binding also affects the equilibrium interlayer distance; the distance between the top two layers of the graphite slab is 3.37 Å, intermediate between the values of 3.39 Å in BLG and 3.35 Å in bulk graphite.

Figure 1(c) shows a comparison of the potential energy surfaces for sliding of the upper graphene layer in BLG and on the graphite surface. Both of the PES show two minima, which are equivalent for BLG and nearly degenerate for graphite. The global minimum-energy configuration, shown in Figure 2(a), corresponds to the zero of energy for the interlayer-

Figure 1: Comparison of the potential energy surfaces for (a) exfoliation and (c) sliding of the upper graphene layer in BLG and on a graphite surface. In (b) and (d), the PES are decomposed in to the XDM-dispersion (solid lines) and base-functional (dashed lines) contributions.

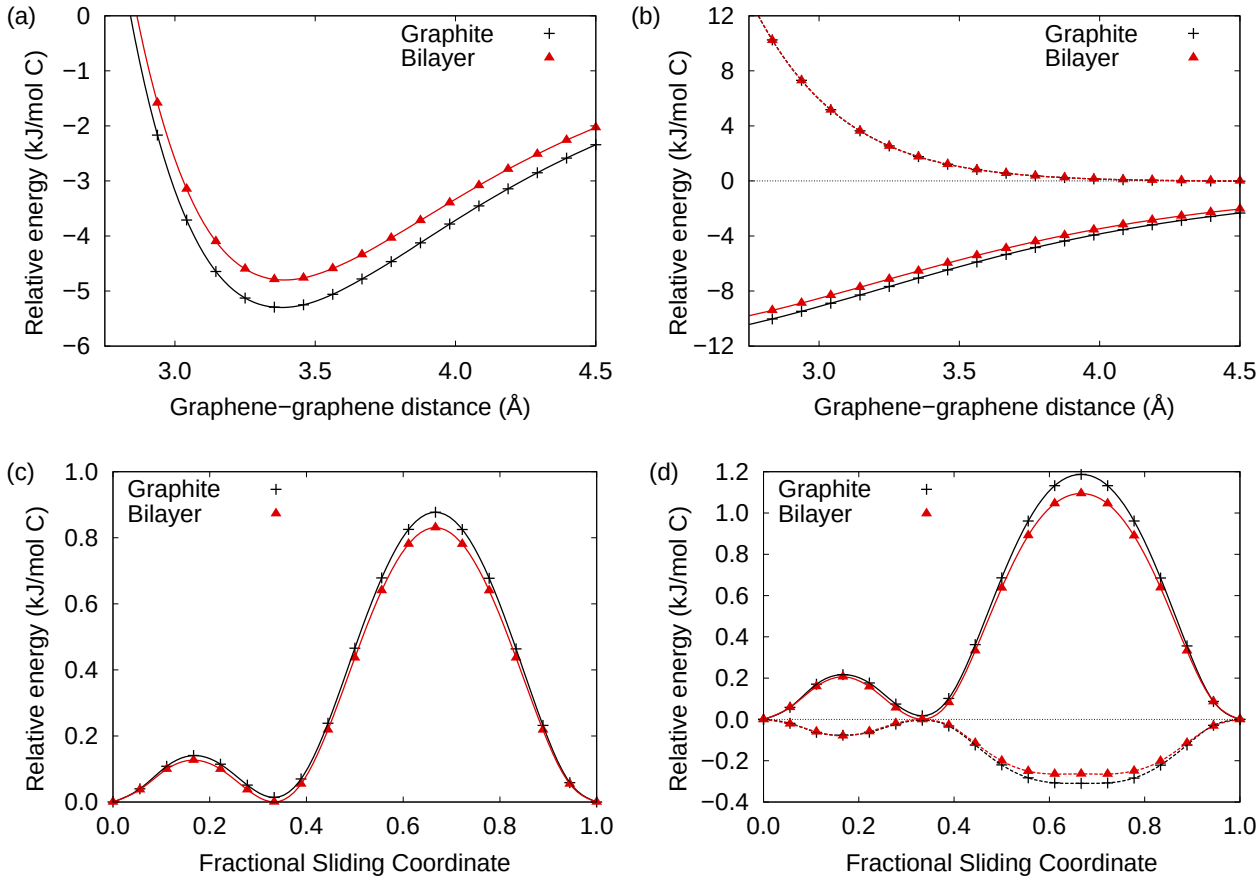

sliding PES. For graphite, this is the "ABA" Bernal stacking seen experimentally.[55,56] The local minimum corresponds to "ABC" stacking, shown in Figure 2(b), and occurs one third of the way along the fractional sliding coordinate. ABC stacking is marginally higher in energy than ABA stacking due to slightly weaker dispersion stabilization. The maximum-energy point on the sliding PES occurs two thirds of the way along the fractional sliding coordinate. As shown in Figure 2(c), this transition state has "AA" stacking, where the top two graphene layers are exactly aligned.

The sliding PES are decomposed into base-functional and dispersion contributions in Figure 1(d). Note that this plot shows the various energy terms at the B86bPBE-XDM optimized geometries and will not match the sliding potential for an uncorrected generalized-

Figure 2: Geometries of three extrema on the sliding PES for graphite. The top two graphene layers are shown in the "tube" representation; black is the upper layer and grey the lower layer. The underlying substrate is represented by the "ball" motif. The green atoms constitute the third carbon layer, or the top of the graphite substrate. The purple atoms are the fourth carbon layer, or the second layer of the graphite substrate.

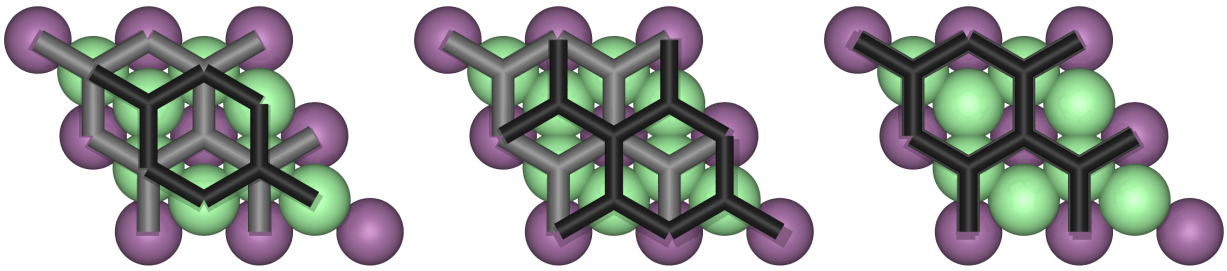

(a) global minimum (b) local minimum (c) maximum

gradient functional in the absence of a dispersion correction. The figure reveals that the sliding barrier is primarily controlled by the XDM dispersion contribution. The AA orientation, where the carbon atoms in the two graphene sheets lie directly above each other (as in Figure 2(c)), gives rise to less dispersion attraction than when they are staggered, as in the AB orientations shown in Figure 2(a,b). The dispersion-only barrier is even somewhat higher than the overall barrier because the base functional contribution favors the stacked AA orientation. To understand the reason for this behavior, recall from Figure 1(b) that the base-functional contribution to the adsorption energy is purely repulsive at all points along the PES, while the dispersion contribution is purely attractive. At the local minima (AB orientations) on the sliding PES, there is greater dispersion binding, leading to a shorter interlayer distance (3.37Å for graphite and 3.38Å for BLG), and this is offset by greater repulsion from the base functional. Conversely, at the maximum (AA orientation), there is less dispersion binding, leading to a longer interlayer distance (3.57Å for graphite and 3.58Å for BLG), so this results in less repulsion from the base functional.

From Figure 1(c,d), the graphite substrate does not significantly affect the sliding PES. The upper graphene layer is far enough from the substrate that the additional dispersion attraction from interaction with the support is largely invariant with respect to its translation. This result is expected since it is well established that graphene rippling, and not other

electronic effects, is the dominant factor that causes the observed reduction in interlayer friction with increasing numbers of graphene layers.[20,22,23]

3.2 Exfoliation

The previous section showed that a graphite base increases the BLG exfoliation energy. In this section, we investigate the exfoliation energy of the upper graphene layer of BLG adsorbed on the various metal surfaces. The resulting interlayer distances and exfoliation energies are reported in Table 2 and the exfoliation PES are illustrated in the first column of Figure 3. Results for graphite are also included as a reference to gauge how each metal affects the exfoliation energy. The dispersion energies along the PES for interactions between the upper graphene layer and the metal are shown in the second column of Figure 3. These results are expressed relative to analogous energies for graphite, where only the interaction between the upper layer and the substrate base are included in the dispersion energy. As such, the curves represent the additional dispersion stabilization gained by replacing the graphite substrate with a given metal surface.

The results in Table 2 show that the interlayer distances and energies are nearly equivalent for all metals in the $(\sqrt{3} \times \sqrt{3})$ cell. All BLG distances are within 0.01 Å of graphite and most exfoliation energies are similar to graphite, differing by no more than 0.3 kJ/mol C. The dispersion contributions from the substrate are also quite similar to graphite, except for Al, which has the lowest dispersion coefficient of the metals considered here.[16]

The results for physisorbed BLG in the (1×1) cell are similar to those for the $(\sqrt{3} \times \sqrt{3})$ cell; the exfoliation energies and distances, again, vary little from those seen for graphite. The dispersion contributions follow the same ordering as the C_6 dispersion coefficients for the metals,[16] namely Al < Cu < Au < Ag. The C_6 coefficients increase down the periodic group, except for gold, where relativistic effects increase the electronegativity and reduce the dispersion coefficient.[57] The slight increases in the surface dispersion contributions relative to graphite (between 0.2-0.4 kJ/mol per C) are offset by the increased graphene strain in

Table 2: Optimum BLG interlayer distances (d_{BLG}), distances between the top graphene layer and the upper layer of the metal surface ($d_{\mathrm{M-top}}$), and graphene adsorption energies (E_{ads}). Relative values, with respect to results for the graphite surface, are also shown. All distances are given in Å and all energies in kJ/mol C.

		d_{BLG}	Δd_{BLG}	$d_{\mathrm{M-top}}$	$\Delta d_{\mathrm{M-top}}$	E_{ads}	ΔE_{ads}
Al	1×1 top-hcp	3.39	0.02	6.87	0.38	5.1	-0.2
	$\sqrt{3} \times \sqrt{3}$	3.37	0.00	7.12	0.63	5.0	-0.3
Cu	1×1 top-fcc	3.38	0.01	6.60	0.11	5.3	0.0
Ag	1×1 top-fcc	3.39	0.02	6.45	-0.04	5.4	0.1
	$\sqrt{3} \times \sqrt{3}$	3.37	-0.01	6.68	0.19	5.3	0.0
Au	1×1 top-fcc	3.40	0.03	6.62	0.13	5.4	0.1
	$\sqrt{3} \times \sqrt{3}$	3.38	0.01	6.79	0.30	5.5	0.2
Ni	1×1 top-fcc	3.29	-0.08	5.51	-0.98	6.2	0.9
Pd	1×1 bridge-top	3.33	-0.04	5.45	-1.04	5.9	0.6
	1×1 top-fcc	3.32	-0.05	5.57	-0.92	5.9	0.6
	$\sqrt{3} \times \sqrt{3}$	3.36	-0.01	6.60	0.11	5.5	0.2
Pt	1×1 bridge-top	3.30	-0.07	5.40	-1.09	6.3	1.0
	1×1 top-fcc	3.30	-0.07	5.70	-0.79	6.0	0.7
	$\sqrt{3} \times \sqrt{3}$	3.36	-0.01	6.80	0.31	5.4	0.1
BLG		3.39	0.02	—	—	4.8	-0.5
Graphite		3.37	—	6.49	—	5.3	—

this cell, resulting in negligible overall changes in the exfoliation PES. Thus, our results show that rotational orientation and lattice commensurability have little affect on BLG exfoliation energies when the BLG is physisorbed on Cu-group metals.

Graphene chemisorbs on Ni, Pd and Pt in the (1×1) cell and, therefore, the graphene-metal interlayer distances are much shorter for these metals.[34] Figure 3 and Table 2 show that the exfoliation energies are somewhat higher when BLG is adsorbed on these metals, by up to 1 kJ/mol C for Pt when the lower graphene layer is chemisorbed in the bridge-top orientation. The stronger interlayer interactions also manifest in the BLG interlayer distances, which are up to 0.08 Å shorter than in graphite. The additional binding can be attributed to a higher dispersion contribution from the substrate, due to the much shorter distances between the top graphene layer and the surface (0.8-1.1Å in Table 2). Thus, dispersion contributions from the underlying substrate can significantly affect the strength of the interlayer interactions in

Figure 3: PES for exfoliation of graphene from a graphene-metal or graphite base (left column). Also shown are dispersion energies for interaction between the exfoliated graphene layer and the metal slab, relative to analogous values for graphite (right column).

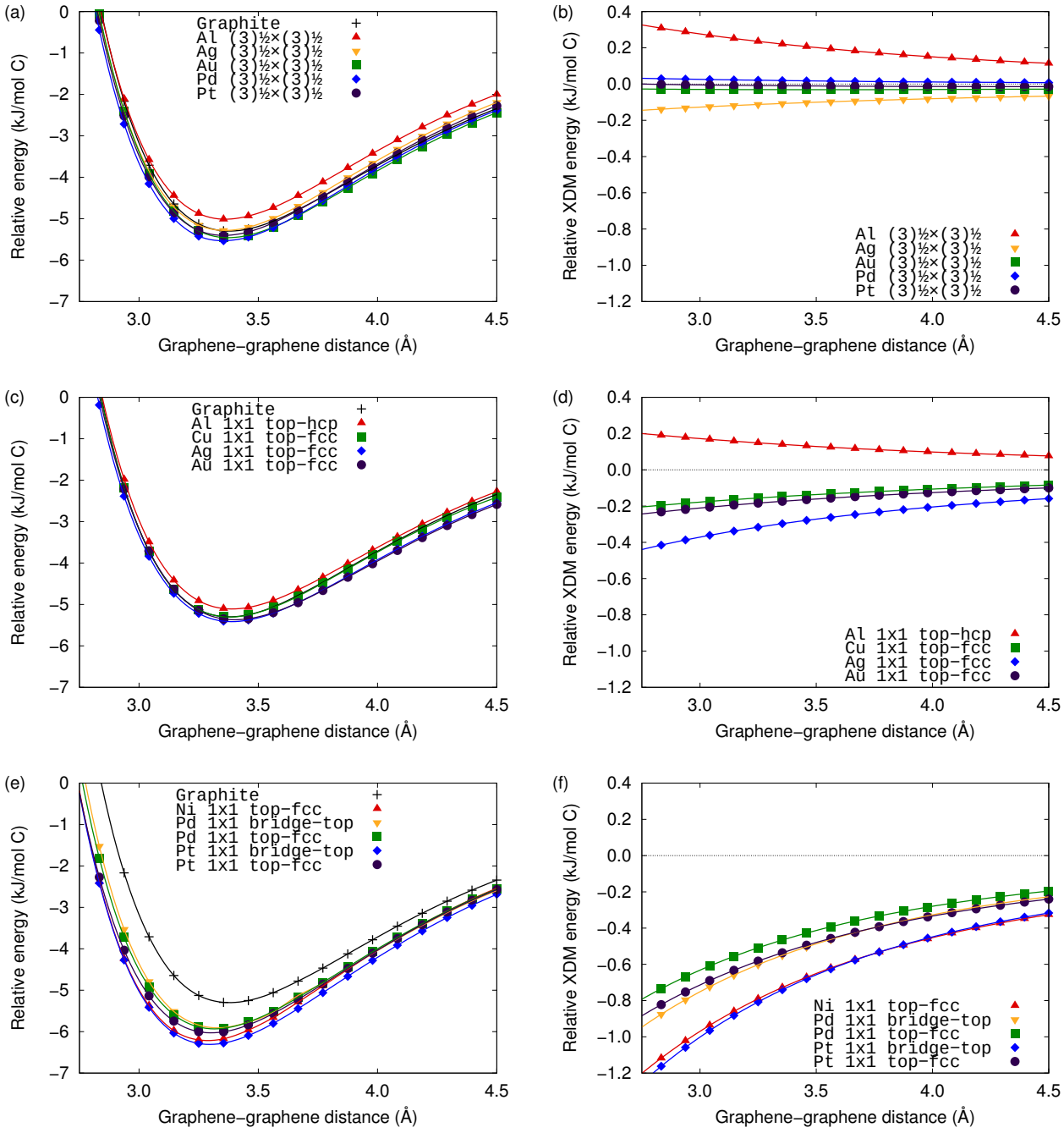

BLG when it is chemisorbed on a metal surface; such substrates should not be neglected in computational modeling.

Finally, we compare our results with those of Wang *et al.*[33] obtained using PBE-D2,[31,32]

who reported exfoliation energies of 5.8, 4.8, and 8.2 kJ/mol C for freestanding BLG and BLG adsorbed on Cu and Ni substrates, respectively. Their result for freestanding BLG is counter-intuitive as it is not physical to have a weakening of the BLG interlayer interaction when it is adsorbed on a substrate. In the limit of extremely weak adsorption, the substrate would have no effect, and the lower bound for the interlayer interaction energy would match that of freestanding BLG. For stronger adsorption, the substrate will contribute additional dispersion interactions to the interlayer binding, so the interlayer interaction energy must increase. To test their prediction, we calculated the exfoliation energy of freestanding BLG with PBE-D2 and obtained a value of 4.8 kJ/mol C, in agreement with our B86bPBE-XDM value in Table 2, as well with the result of Ref. 33 for BLG on Cu. We conjecture that the reported values in Ref. 33 for freestanding BLG and for BLG adsorbed on the Cu surface may have been switched accidentally. If this were indeed the case, the PBE-D2 exfoliation energy for BLG on Cu would be slightly higher than the corresponding XDM result, which is reasonable given the tendency of the D2 method to overestimate dispersion interactions for metals.[37] For BLG adsorbed on Ni, our calculated interlayer interaction energy is 2 kJ/mol C lower than that obtained in Ref. 33. This is expected due to the tendency of the empirical D2 method to overestimate dispersion interactions with Ni due to an overestimated Ni-C C_6 dispersion coefficient (75.4 a.u. with D2[32] versus 39.3 a.u. with XDM[16]). This overestimation of C_6 will cause the "extra" dispersion contribution from the substrate to be overestimated, explaining the difference between the two sets of results.

3.3 Graphene Sliding

Graphene sliding PES are reported on the left side of Figure 4; the panels on the right show only the XDM dispersion contribution to the sliding PES. Figure 4(a) shows the PES for interlayer sliding of BLG adsorbed on metal substrates in the $(\sqrt{3}\times\sqrt{3})$ cell. The computed sliding barrier is highest for gold, which has the largest lattice mismatch with BLG, as shown in Table 1.

To investigate the effect of lattice mismatch on the sliding barriers, additional calculations were performed on freestanding BLG with a series of lattice constants spanning the full range of a_{surf} values listed in Table 1. The results are illustrated by a 2D representation of the sliding PES as a function of the lattice constant in Figure 5(a). The figure shows that stretching of the graphene lattice constant beyond the equilibrium value of 2.47 Å serves to increase the sliding barrier (from 0.8 kJ/mol C to 1.1 kJ/mol C over the range considered). Figures 5(b,c) present the decomposition of the 2D PES into base-functional and dispersion contributions. The dispersion contribution to the barrier is largely constant and the increase in sliding barrier with lattice constant is shown to originate from changes in the base-functional repulsion between the layers. Stretching the lattice constant beyond the BLG equilibrium value decreases base-functional repulsion between the graphene layers for the minimum-energy AB configuration, but increases base-functional repulsion for the maximum-energy AA configuration. The net result is a higher sliding barrier due this change in the base-functional contribution.

As shown in Figure 4(c), the sliding PES for the (1×1) cell exhibit a larger spread between the various metals than for the $(\sqrt{3} \times \sqrt{3})$ cell. This occurs because of the greater range of lattice constants and increasing strain for BLG on the (1×1) surfaces (see Table 1). Physisorption on the (1×1) Ag and Au surfaces causes the greatest lattice mismatch and hence the highest sliding barriers. Conversely, for Cu in the (1×1) cell, there is almost no lattice mismatch and, consequently, the sliding barrier for BLG on this surface is almost identical to that for graphite. Al has an intermediate lattice mismatch, but the increase in barrier from the base functional is offset by a lower dispersion contribution, as shown in Figure 4(d) and as expected due to the reduced dispersion binding for BLG on Al compared to the other metals.

The PES shown in Figure 4(e), for cases where BLG is chemisorbed on the metal substrate in the top-fcc orientation, are significantly different than those discussed above. The global and local minima, shown in Figure 6(a,b), are no longer nearly degenerate. Rather, the

Figure 4: PES for sliding of the upper graphene layer over a fixed graphene-metal or graphite base, along the long diagonal of the unit cell, with the z-position of the translated layer allowed to relax. The left column shows the total sliding PES and the right column shows the XDM dispersion contribution only; both are relative to the lowest-energy orientation.

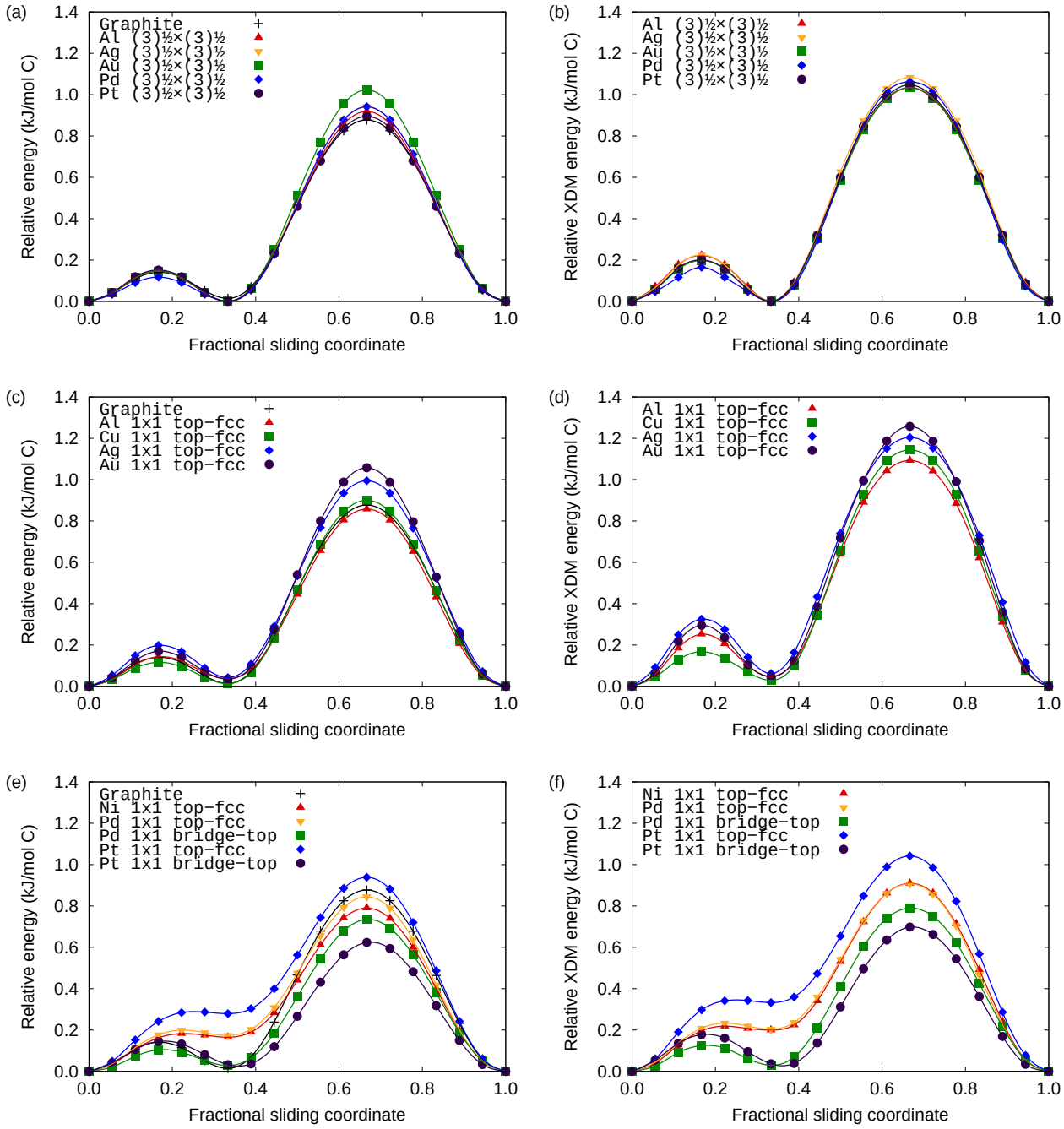

local minimum, in which the upper graphene layer is translated one third of the way across the unit cell, is significantly higher in energy. At the local minimum, the carbon atoms of the upper graphene layer lie directly above the surface metal atoms. This can be contrasted

Figure 5: 2D PES illustrating the dependence of BLG interlayer sliding on the lattice constant. The total BLG interaction energy (a), as well as the XDM-dispersion (b), and base-functional (c) contributions are shown.

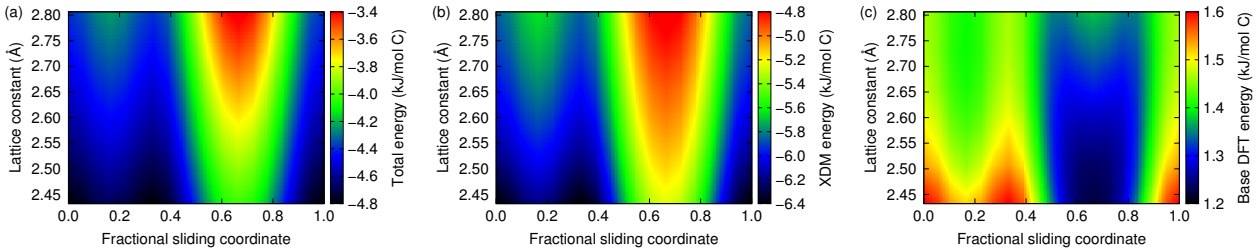

with the global minimum, where the carbons of the upper layer lie between the surface metal atoms. The latter arrangement results in more close carbon-metal contacts and consequently greater dispersion stabilization. However, it is only for the chemisorbed cases where the upper graphene layer is sufficiently close to the surface (see Table 2) for this difference to be significant. The destabilization of the local minimum is not seen for the bridge-top orientations as this breaks the symmetry between the lower graphene layer and the surface. The global and local minima, shown in Figure 6(d,e), are nearly degenerate. In the first case the C-C bonds lie above metal atoms of the second surface layer (cyan) resulting in greater stabilization from dispersion interactions, while in the second case, the C-C bonds lie above the metal atoms of the third surface row (dark blue).

For the chemisorbed cases (Figure 4(e)) the sliding energy barriers are much lower than for the physisorbed cases and this arises from the dispersion contribution (Figure 4(f)). The additional dispersion from the substrate causes a reduction in the graphene interlayer distance, by 0.08 Å or less at the minimum-energy configuration. At the maximum-energy configuration, the contraction in the interlayer distance is as much as 0.18 Å. This reduction in the interlayer distance serves to preferentially increase the dispersion attraction between the two graphene layers at the maximum-energy configuration, lowering the barrier. The finding that chemisorption of BLG on a metal surface simultaneously increases the interlayer adhesion and decreases the sliding friction is a generalization of the previous PBE-D2 results for Ni(111) in Ref. 7.

Figure 6: Geometries of the extrema on the sliding PES for BLG adsorbed on Cu in the top-fcc orientation (top row) or Pt in the bridge-top orientation (bottom row). The top two graphene layers are shown in the "tube" representation; black is the upper layer and grey the lower layer. The underlying substrate is represented by the "ball" motif.

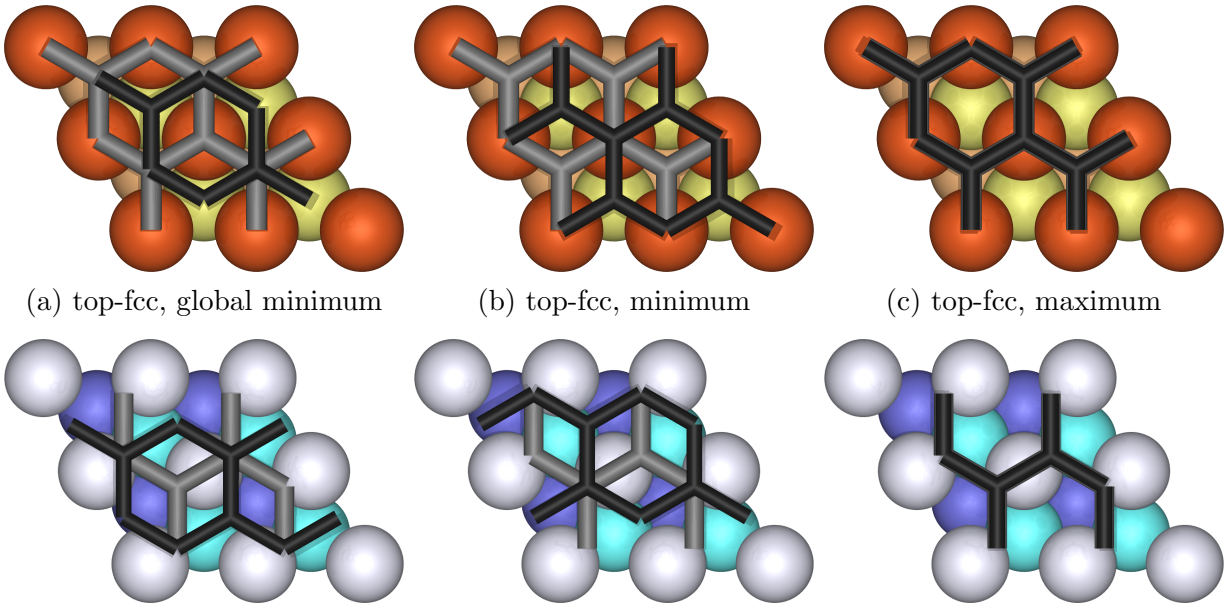

(a) top-fcc, global minimum (b) top-fcc, minimum (c) top-fcc, maximum

(d) bridge-top, global minimum (e) bridge-top, local minimum (f) bridge-top, maximum

The sliding barriers for chemisorbed BLG are also particularly sensitive to the translational orientation of the lower graphene layer with respect to the surface. Relative to the top-fcc orientation discussed above, the sliding barriers are further reduced for the bridge-top orientation, due to more preferable dispersion interactions between the top graphene layer and the metal surface at the transition state. For the top-fcc orientation, the transition state has an all-aligned AAA configuration for the BLG and top layer of surface atoms, as in Figure 4(c). This can be contrasted with the transition state for the bridge-top orientation in Figure 4(f), in which the carbon atoms lie between the atoms of the top metal layer, resulting in more favorable dispersion interactions.

The results for the sliding barriers are qualitatively similar to exfoliation energies, in that physisorption effects are negligible, while chemisorption can significantly perturb the interlayer interactions. While the substrate contributes additional dispersion interactions not present in free BLG, the added dispersion is relatively constant with respect to translation for

physisorbed BLG and thus will have little effect on the sliding barrier. The variations between substrates are instead due to changes in the surface lattice constant, which stretches the BLG and consequently affects the base functional repulsion between the layers. However, this is an artifact of the highly-strained unit cells employed in the calculations (to ensure commensurate lattice constants) and will be mediated in real systems by the adoption of different rotational orientations by the graphene to minimize lattice strain. Thus, sliding of physisorbed BLG is effectively independent of the choice of substrate. However, for chemisorbed BLG, the effect of the substrate is much more significant and can lower the dispersion contribution to the barrier by as much as 40%. Moreover, the translational orientations of the chemisorbed BLG strongly affect the frictional behavior.

4 Summary

This paper investigated the effects of substrates on BLG interlayer interactions, as quantified by exfoliation energies and sliding-energy barriers. The substrates studied were face-centered cubic metal (111) surfaces of Al, Cu, Ag, Au, Ni, Pd, and Pt; a graphite substrate and freestanding BLG were also considered as reference systems for comparison. Potential-energy surfaces for exfoliation and translation of the top graphene layer were calculated using the B86bPBE exchange-correlation functional and the exchange-hole dipole moment (XDM) dispersion correction.

In the first section, we showed how the exfoliation energies and sliding barriers differ between graphite and BLG. The addition of a graphite support increases the exfoliation energy by 0.5 kJ/mol C, due to the added dispersion interactions between the top graphene layer and the substrate. However, the sliding PES for the two systems are almost equivalent, as this additional dispersion is effectively constant with respect to translation of the upper graphene layer.

Physisorption of BLG on metal substrates results in similar exfoliation energies and

sliding barriers to graphite. The BLG sliding barriers are sensitive to the surface lattice constant, with greater lattice strain resulting in higher friction. However, this is an artifact of enforcing commensurate lattices in our calculations, resulting in highly strained graphene in some cases. In practice, the graphene can adopt differing rotational orientations to minimise lattice strain.

Chemisorption of BLG occurs for differing rotational orientations on Ni-group metals and results in shorter interlayer distances and increased dispersion attraction between the top graphene layer and the metal surface. The closer proximity to the substrate increases the BLG exfoliation energy by $\sim 20\%$ relative to graphite. Dispersion attraction to the substrate preferentially stabilizes the maximum-energy "AA" stacked orientation of BLG, reducing sliding barriers by up to $\sim 30\%$. Additionally, when BLG is chemisorbed on a metal substrate, changes in the translational orientations of the BLG with respect to the surface can alter the sliding barriers by as much as $\sim 50\%$. These results demonstrate the need to explicitly include dispersion contributions from the substrate in computational studies of chemisorbed BLG.

Acknowledgement

We gratefully acknowledge the Natural Sciences and Engineering Research Council of Canada (NSERC) for financial support and Compute Canada (ACEnet and Westgrid) for computational resources.

Supporting Information Available

Exfoliation PES using fixed, experimental surface lattice constants for each metal. This material is available free of charge via the Internet at `http://pubs.acs.org/`.

References

(1) Park, H. J.; Meyer, J.; Roth, S.; Skákalová, V. Growth and properties of few-layer graphene prepared by chemical vapor deposition. *Carbon* **2010**, *48*, 1088.

(2) Bartelt, N.; McCarty, K. Graphene growth on metal surfaces. *MRS Bull.* **2012**, *37*, 1158–1165.

(3) Dahal, A.; Addou, R.; Sutter, P.; Batzill, M. Graphene monolayer rotation on Ni(111) facilitates bilayer graphene growth. *Appl. Phys. Lett.* **2012**, *100*, 241602.

(4) Muñoz, R.; Gómez-Aleixandre, C. Review of CVD synthesis of graphene. *Chem. Vap. Depos.* **2013**, *19*, 297.

(5) Zhang, Y.; Zhang, L.; Zhou, C. Review of chemical vapor deposition of graphene and related applications. *Acc. Chem. Res.* **2013**, *46*, 2329.

(6) Dahal, A.; Batzill, M. Graphene-nickel interfaces: a review. *Nanoscale* **2014**, *6*, 2548.

(7) Cahangirov, S.; Ciraci, S.; Özçelik, V. O. Superlubricity through graphene multilayers between Ni(111) surfaces. *Phys. Rev. B - Condens. Matter Mater. Phys.* **2013**, *87*, 205428.

(8) Penkov, O.; Kim, H. J.; Kim, H. J.; Kim, D. E. Tribology of graphene: A review. *Int. J. Precis. Eng. Manuf.* **2014**, *15*, 577–585.

(9) Tripathi, M. et al. Tribological characteristics of few-layer graphene over Ni grain and interface boundaries. *Nanoscale* **2016**, *8*, 6646–6658.

(10) Wintterlin, J.; Bocquet, M. L. Graphene on metal surfaces. *Surf. Sci.* **2009**, *603*, 1841–1852.

(11) Swart, J. C. W.; van Steen, E.; Ciobíc, I. M.; van Santen, R. a. Interaction of graphene with FCC–Co(111). *Phys. Chem. Chem. Phys.* **2009**, *11*, 803–807.

(12) Nie, S.; Wofford, J. M.; Bartelt, N. C.; Dubon, O. D.; McCarty, K. F. Origin of the mosaicity in graphene grown on Cu(111). *Phys. Rev. B* **2011**, *84*, 155425.

(13) Wofford, J. M. et al. Extraordinary epitaxial alignment of graphene islands on Au(111). *New J. Phys.* **2012**, *14*, 053008.

(14) Gamo, Y.; Nagashima, A.; Wakabayashi, M.; Terai, M.; Oshima, C. Atomic Structure of Monolayer Graphite Formed on Ni(111). *Hyomen Kagaku* **1996**, *17*, 745–749.

(15) Gao, L.; Guest, J. R.; Guisinger, N. P. Epitaxial Graphene on Cu(111). *Nano Lett.* **2010**, *10*, 3512–3516.

(16) Christian, M. S.; Otero-de-la Roza, A.; Johnson, E. R. Adsorption of graphene to metal (111) surfaces using the exchange-hole dipole moment model. *Carbon* **2017**, *124*, 531–540.

(17) Lee, C. et al. Elastic and frictional properties of graphene. *Phys. Status Solidi* **2009**, *246*, 2562–2567.

(18) Filleter, T.; Bennewitz, R. Structural and frictional properties of graphene films on SiC(0001) studied by atomic force microscopy. *Phys. Rev. B* **2010**, *81*, 1–7.

(19) Kitt, A. L. et al. How Graphene Slides: Measurement and Theory of Strain- Dependent Frictional Forces between Graphene and SiO2. *Nano Lett.* **2013**, *13*, 2605–2610.

(20) Cho, D.-H. et al. Effect of surface morphology on friction of graphene on various substrates. *Nanoscale* **2013**, *5*, 3063.

(21) Zhang, H.; Guo, Z.; Gao, H.; Chang, T. Stiffness-dependent interlayer friction of graphene. *Carbon* **2015**, *94*, 60–66.

(22) Li, Q.; Lee, C.; Carpick, R. W.; Hone, J. Substrate effect on thickness-dependent friction on graphene. *Phys. Status Solidi Basic Res.* **2010**, *247*, 2909–2914.

(23) Ye, Z.; Balkanci, A.; Martini, A.; Baykara, M. Z. Effect of roughness on the layer-dependent friction of few-layer graphene. *Phys. Rev. B* **2017**, *96*, 1–6.

(24) Coffey, T.; Krim, J. Impact of substrate corrugation on the sliding friction levels of adsorbed films. *Phys. Rev. Lett.* **2005**, *95*, 076101.

(25) Walker, M.; Jaye, C.; Krim, J.; Cole, M. W. Frictional temperature rise in a sliding physisorbed monolayer of Kr/graphene. *J. Phys. Condens. Mat.* **2012**, *24*, 424201.

(26) Chen, Z. et al. Physical adsorption and charge transfer of molecular Br2 on graphene. *ACS Nano* **2014**, *8*, 2943–2950.

(27) Lodge, M. S. et al. Lubricity of gold nanocrystals on graphene measured using quartz crustal microbalance. *Sci. Rep.* **2016**, *6*, 31837.

(28) Zheng, J. et al. Interfacial Properties of Bilayer and Trilayer Graphene on Metal Substrates. *Sci. Rep.* **2013**, *3*, 2081.

(29) Bian, X. et al. Graphene layers on bimetallic Ni/Cu(111) surface and near surface alloys in controlled growth of graphene. *RSC Adv.* **2016**, *6*, 74973–74981.

(30) Khan, E.; Rahman, T. S.; Subrina, S. Electronic structure of bilayer graphene physisorbed on metal substrates. *J. App. Phys.* **2016**, *120*, 185101.

(31) Perdew, J.; Burke, K.; Ernzerhof, M. Generalized gradient approximation made simple. *Phys. Rev. Lett.* **1996**, *77*, 3865–3868.

(32) Grimme, S. Semiempirical GGA-type density functional constructed with a long-range dispersion correction. *J. Comput. Chem.* **2006**, *27*, 1787–1799.

(33) Wang, Q.; Wei, L.; Sullivan, M.; Yang, S.-W.; Chen, Y. Graphene layers on Cu and Ni (111) surfaces in layer controlled graphene growth. *RSC Adv.* **2013**, *3*, 3046–3053.

(34) Christian, M. S.; de-la Roza, A. O.; Johnson, E. R. Adsorption of graphene to nickel (111) using the exchange-hole dipole moment model. *Carbon* **2017**, *118*, 184 – 191.

(35) Becke, A. D.; Johnson, E. R. Exchange-hole dipole moment and the dispersion interaction revisited. *J. Chem. Phys.* **2007**, *127*, 154108.

(36) Johnson, E. R. In *Non-covalent Interactions in Quantum Chemistry and Physics*; Otero-de-la Roza, A., DiLabio, G. A., Eds.; Elsevier, 2017; Chapter 5, pp 169–194.

(37) Christian, M. S.; Otero-De-La-Roza, A.; Johnson, E. R. Surface adsorption from the exchange-hole dipole moment dispersion model. *J. Chem. Theory Comput.* **2016**, *12*, 3305.

(38) Blöchl, P. E. Projector augmented-wave method. *Phys. Rev. B* **1994**, *50*, 17953.

(39) Giannozzi, P.; Baroni, S.; et. al., QUANTUM ESPRESSO: a modular and open-source software project for quantum simulations of materials. *J. Phys. Condens. Mat.* **2009**, *21*, 395502.

(40) Becke, A. D. On the large-gradient behavior of the density functional exchange energy. *J. Chem. Phys.* **1986**, *85*, 7184.

(41) Otero-de-la-Roza, A.; Johnson, E. R. Van der Waals interactions in solids using the exchange-hole dipole moment. *J. Chem. Phys.* **2012**, *136*, 174109.

(42) Otero-de-la-Roza, A.; Johnson, E. R. A benchmark for non-covalent interactions in solids. *J. Chem. Phys.* **2012**, *137*, 054103.

(43) Marzari, N.; Vanderbilt, D.; De Vita, A.; Payne, M. C. Thermal Contraction and Disordering of the Al(110) Surface. *Phys. Rev. Lett.* **1999**, *82*, 3296.

(44) Gao, J. H.; Ishida, N.; Scott, I.; Fujita, D. Controllable growth of single-layer graphene on a Pd(111) substrate. *Carbon* **2012**, *50*, 1674–1680.

(45) Gao, M. et al. Epitaxial growth and structural property of graphene on Pt(111). *Appl. Phys. Lett.* **2011**, *98*, 3–6.

(46) Sutter, P.; Sadowski, J. T.; Sutter, E. Graphene on Pt(111): Growth and substrate interaction. *Phys. Rev. B - Condens. Matter Mater. Phys.* **2009**, *80*, 1–10.

(47) Sasaki, M.; Yamada, Y.; Ogiwara, Y.; Yagyu, S.; Yamamoto, S. Moiré contrast in the local tunneling barrier height images of monolayer graphite on Pt(111). *Phys. Rev. B* **2000**, *61*, 15653–15656.

(48) Martínez-Galera, A. J.; Brihuega, I.; Gómez-Rodríguez, J. M. Ethylene irradiation: A new route to grow graphene on low reactivity metals. *Nano Lett.* **2011**, *11*, 3576–3580.

(49) Kwon, S. Y. et al. Growth of semiconducting graphene on palladium. *Nano Lett.* **2009**, *9*, 3985–3990.

(50) Murata, Y. et al. Orientation-dependent work function of graphene on Pd(111). *Appl. Phys. Lett.* **2010**, *97*, 2014–2017.

(51) Merino, P.; Svec, M.; Pinardi, A. L.; Otero, G. Strain-Driven Moire Superstructures of Epitaxial Graphene on Transition. *ACS Nano* **2011**, *5*, 5627–5634.

(52) Ueta, H. et al. Highly oriented monolayer graphite formation on Pt(111) by a supersonic methane beam. *Surf. Sci.* **2004**, *560*, 183–190.

(53) Chan, N. et al. Contrast in nanoscale friction between rotational domains of graphene on Pt(111). *Carbon* **2017**, *113*, 132–138.

(54) Johnson, E. R.; Mackie, I. D.; DiLabio, G. A. Dispersion interactions in density-functional theory. *J. Phys. Org. Chem.* **2009**, *22*, 1127–1135.

(55) Lui, C. H. et al. Imaging stacking order in few-layer graphene. *Nano Lett.* **2011**, *11*, 164–169.

(56) Malard, L. M.; Pimenta, M. A.; Dresselhaus, G.; Dresselhaus, M. S. Raman spectroscopy in graphene. *Phys. Rep.* **2009**, *473*, 51–87.

(57) Otero-de-la-Roza, A.; Mallory, J. D.; Johnson, E. R. Metallophilic interactions from dispersion-corrected density-functional theory. *J. Chem. Phys.* **2014**, *140*, 18A504.

Graphical TOC Entry